Journal of Power Sources 186 (2009) 268–277

Contents lists available at ScienceDirect

Journal of Power Sources

journal homepage: www.elsevier.com/locate/jpowsour

Structural, morphological and electrical properties of $Gd_{0.1}Ce_{0.9}O_{1.95}$ prepared by a citrate complexation method

Rodolfo O. Fuentes [1], Richard T. Baker *

School of Chemistry, University of St. Andrews, North Haugh, KY16 9ST St. Andrews, Fife, United Kingdom

ARTICLE INFO

Article history:
Received 31 July 2008
Received in revised form
10 September 2008
Accepted 28 September 2008
Available online 17 October 2008

Keywords:
Cation complexation
IT-SOFC
Solid electrolytes
Gadolinium-doped ceria
Ionic conductivity

ABSTRACT

A variant of the sol–gel technique known as cation complexation is used to prepare a nanocrystalline $Gd_{0.1}Ce_{0.9}O_{1.95}$ (GDC) solid solution. A range of techniques including thermal analysis (TGA/DTA), X-ray diffraction, specific surface area determination (BET) and electron microscopy (SEM and TEM) are employed to characterise the GDC powders. GDC calcined at 500 °C is found to have an average crystallite size of 11 nm. Specific surface areas are found to be 29.7 $m^2\,g^{-1}$ for the as-calcined powder and 57.5 $m^2\,g^{-1}$ after ball milling at 400 rpm. Dense ceramic pellets are prepared from unmilled and ball-milled GDC powders employing different thermal treatments. Their electrical properties are studied by impedance spectroscopy. Those samples sintered at 1300 °C for 30 h (starting from ball-milled powders) exhibit the highest density (96% of theoretical density) and the highest total ionic conductivity (1.91×10^{-2} S cm^{-1} at 600 °C).

1. Introduction

Ceria and rare earth-doped ceria powders have a number of important applications in catalysts, abrasives, solid oxide fuel cell (SOFC) systems and gas sensors. Alkaline earth and rare earth oxides have high solubilities in cerium oxide and readily form substitutional solid solutions. The introduction of aliovalent cations gives rise to oxygen vacancies as charge compensating defects thereby enhancing the ionic conductivity of these materials. The ionic conductivity of Gadolinia-doped ceria solid solution is one of the highest among this class of solid electrolytes. For this reason, it is one of the ceria-based solid solutions proposed for intermediate temperature application of SOFCs [1,2]. Ceria (CeO_2) has the fluorite type crystal structure with space group $Fm\bar{3}m$. Aliovalent dopants, such as the rare earth oxides (Y_2O_3, Gd_2O_3, Sm_2O_3, Nd_2O_3, etc.), form solid solutions with ceria and introduce vacancies in the anion sub-lattice as charge compensating defects. The defect reactions can be written in Kroeger–Vink notation as:

$$Gd_2O_3 \xrightarrow{2CeO_2} 2Gd'_{Ce} + 3O_O^x + V_O^{\bullet\bullet} \quad (1)$$

Oxygen ion vacancies ($V_O^{\bullet\bullet}$) are responsible for the ionic conductivity observed in doped ceria [1]. Because of their high ionic conductivity at elevated temperature (above 600 °C), these materials have potential for applications in gas sensors, ceramic oxygen generators, catalytic membranes and electrolytes for SOFCs. However, the magnitude of the electrical conductivity and the stability of Ce^{4+} under reducing atmospheres are greatly dependent on the type and concentration of the dopants.

These ceria-based solid solutions can be synthesised by a variety of techniques such as conventional powder mixing, co-precipitation, and hydrothermal recrystallization. In general, chemical techniques have the advantage over conventional techniques that the precursor possesses high reactivity which allows a reduction in the calcination temperature and/or calcination time [3–6].

A wide variety of processes are available for the synthesis of ceramic powders. Among the various synthetic approaches, solid state synthesis requires a high calcination temperature (above 1000 °C) for the formation of a homogeneous phase. It has been normal practice to repeatedly calcine and grind the powder mixture in order to achieve the desired homogeneity. Therefore, the risk of contamination from the grinding media is greater in this process. In general, however, wet chemical processes are capable of producing high purity, homogeneous and ultrafine powders at lower temperature. The synthesis of ceria powder by various wet chemical routes, such as the co-precipitation, hydrothermal solution and the combustion routes has been reported. In the combustion route

* Corresponding author. Tel.: +44 1334 463899; fax: +44 1334 463808.
E-mail addresses: rfuentes@citefa.gov.ar (R.O. Fuentes), rtb5@st-andrews.ac.uk (R.T. Baker).
[1] Permanent address: CINSO (Centro de Investigaciones en Sólidos), CITEFA-CONICET, J.B. de Lasalle 4397, B1603ALO, Buenos Aires, Argentina.

0378-7753/$ – see front matter © 2008 Elsevier B.V. All rights reserved.
doi:10.1016/j.jpowsour.2008.09.119

a self-sustaining exothermic redox reaction between a fuel (such as a polycarboxylic acid) and an oxidant (nitrate salts of metals) is allowed to take place. The fuel also acts as a complexing agent in the aqueous solution of nitrate salts. On heating the solution a gel is formed as an intermediate before the combustion reaction starts. Hence, the process is also known as gel combustion. The gas evolution in the combustion process helps in limiting the inter-particle contact and thus results in ultrafine powders. The synthesis of ultrafine powder is of particular importance in order to obtain a dense sintered product at a sintering temperature that is lower than that at which change of the valence state of cerium ($Ce^{4+} \rightarrow Ce^{3+}$) starts [7].

Earlier work using polymeric precursor techniques for the preparation of ceria solid electrolytes have shown that it was necessary to employ high temperatures (>1500 °C) and long sintering times (>5 h), or to introduce a milling step after calcination, to attain a high densification. In these previous studies, the polymeric precursor was prepared by the Pechini method using tartaric acid and ethylene glycol, or citric acid and ethylene glycol, for the polymerization [8]. Alternatively, an organic precursor can be prepared by using ethylene glycol as a complexing agent without the polyesterification reaction [9,10].

Previous studies indicated that small amounts of Fe_2O_3 (0.5 at.%) or Co_2O_3 (2 mol%) are extremely effective in promoting densification of GDC samples at relative low temperatures (<1300 °C) without any negative effects on electrical properties [11,12]. A combination of suitable powder processing and a low sintering temperature with addition of Co was used to decrease the ion blocking effects at the grain boundaries [13].

In this work, a variant of the sol–gel technique known as cation complexation, as proposed by Muccillo et al. [10] was used for the preparation of the ceria-gadolinia solid solution. This method has the advantage of low cost and relative simplicity. Moreover, this technique generates less carbon residues than other similar techniques of synthesis, and it has proved to be quite effective for the preparation of highly sinterable ceramic powders. Detailed structural and physical characterisation employing X-ray diffraction (XRD) and scanning and high resolution transmission electron microscopy (SEM and HRTEM) was carried out to evaluate the final nanopowders. Moreover, the electrical properties in sintered samples starting from powders with different processing treatments were studied by impedance spectroscopy (IS).

2. Experimental

$Gd_{0.1}Ce_{0.9}O_{1.95}$ (GDC) was synthesised from nitrate precursors by complexing the metal cations with the citrate ion. Cerium and gadolinium nitrate hexahydrates (99.99%—Aldrich) were employed as precursors. Each nitrate was dissolved in deionised (d.i.) water individually and then these solutions were mixed. Anhydrous citric acid (99.5%—Riedel-deHaën) was dissolved in d.i. water and this was added to the cation solution. The molar ratio of total oxide (TO) to citric acid (CA) was 1:2. After homogenization of this solution, the temperature was raised to 80 °C, and the solution maintained under stirring to remove excess water and to convert it to a transparent gel. While raising the temperature, the solution became more viscous with evolution of foam, and finally it gelled without any visible precipitation or turbidity. During the dwell at 80 °C there was an increase in viscosity and simultaneous elimination of water and NO_2. The initial thermal decomposition of the precursor was carried out at 250 °C for 1 h. The resulting ash-like material was then pyrolyzed at 500, 600 and 800 °C for 1 h at each temperature. Fig. 1 presents a flow diagram of the citrate complexation method employed in this work.

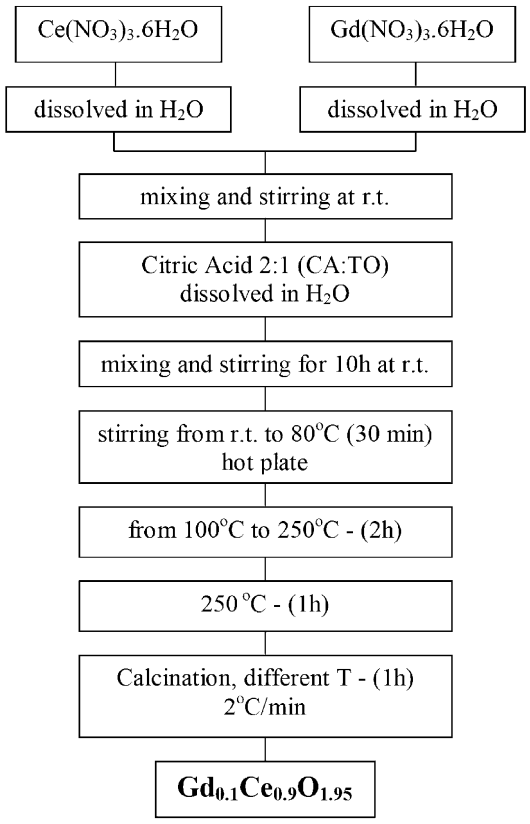

Fig. 1. Flowchart illustrating the synthetic route to nanocrystalline GDC powders via the citrate complexation technique.

Thermal analysis (TGA/DTA) of the gel precursors of GDC was carried out in flowing air at a heating rate of 5 °C min^{-1} up to 800 °C using a Pt crucible in a TA Instruments SDT 2960. Further TGA/DSC runs with analysis of off-gases by mass spectrometry (MS) were carried out in flowing O_2 with a similar set-up, using a Netzsch STA 499 C Jupiter instrument.

The residual carbon content of samples calcined at different temperatures for 1 h was determined by elemental analysis using a Carlo Erba CHNS analyser.

Specific surface area (SSA) measurements were carried out using Brunauer, Emmett and Teller (BET) analysis by nitrogen adsorption (ASAP 2010, Micromeritics).

Calcined powders were studied by XRD using a Philips PW 1710 diffractometer (Cu Kα radiation). Data in an angular region of $2\theta = 20–100°$ were collected in a step-scanning mode (0.02° steps with a step-counting time of 12 s). High-grade silicon powder was used as a standard to allow for the instrument broadening correction.

SEM images were obtained using a Philips XL30 E-SEM instrument with a field emission gun. Transmission electron microscopy (TEM) images and selected area electron diffraction (SAED) patterns of the calcined powders were obtained using a JEOL 2010 TEM instrument. Samples were prepared by dipping a sample grid (copper grids of holey carbon film) into an ultrasonic dispersion of GDC powder in hexane and leaving these to dry overnight.

Part of the calcined powder was dry ground in a 45 cm^3 inner volume Nylon® container using a Fritsch Pulverissette 7 planetary ball mill operated at 400 rpm. Zirconia balls with a diameter of 10 mm were used as the grinding medium with a ball to powder weight ratio of 10:1. The grinding was interrupted at regular intervals (every 10 min) during the whole process to dislodge the powder from the walls of the containers.

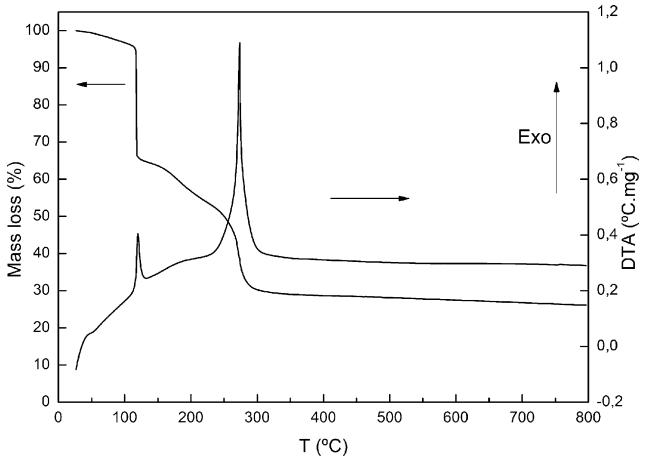

Fig. 2. TGA and DTA plots for the metal nitrate precursors of GDC.

The GDC powder was uniaxially pressed in a 10 mm diameter cylindrical die at 200 MPa. The resulting green pellets were placed in a Pt crucible and sintered in air employing different sintering programs (varying both temperature and time) with a slow heating rate (2 °C min^{-1}) in all cases.

Pt electrodes were deposited on both sides of the dense sintered GDC samples by painting with inorganic-free Pt ink (Engelhardt) and firing at 1000 °C for 1 h. Two probe IS measurements (Solartron 1260) were carried out in dry air in a temperature range between 200 and 800 °C and over a frequency range of 1 Hz to 10 MHz.

3. Results and discussion

3.1. Powder characterization

Fig. 2 shows the TGA/DTA plot (carried out in air) for the GDC gel precursor. The DTA curve exhibits two exothermic peaks, starting at 112 and 234 °C, respectively. The first one can be ascribed to H_2O release. The second exothermic peak can be related to the burn out of organic materials, by liberation of NO_x, CO, CO_2, and to the crystallization of the GDC solid solution [9]. In order to confirm these assignments, it was necessary to employ O_2 as a carrier gas and perform the TGA/DSC experiment with analysis of off-gas using MS. A similar TGA/DTA plot was obtained. The MS data confirmed that H_2O is the main product released in the first exothermic peak

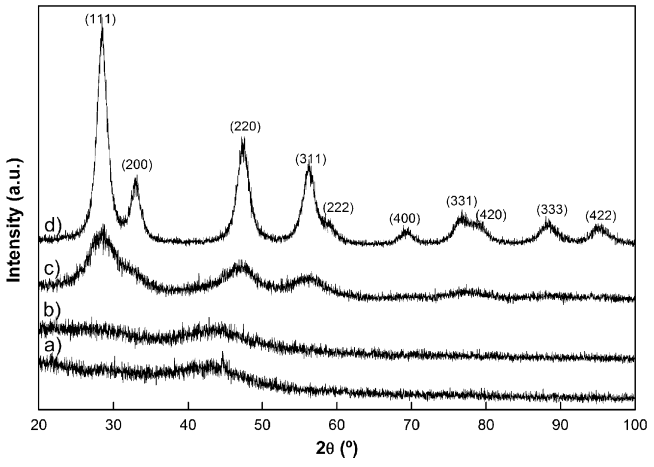

Fig. 3. XRD patterns of the GDC gel precursor calcined at for 1 h at (a) 100 °C, (b) 150 °C, (c) 200 °C and (d) 250 °C.

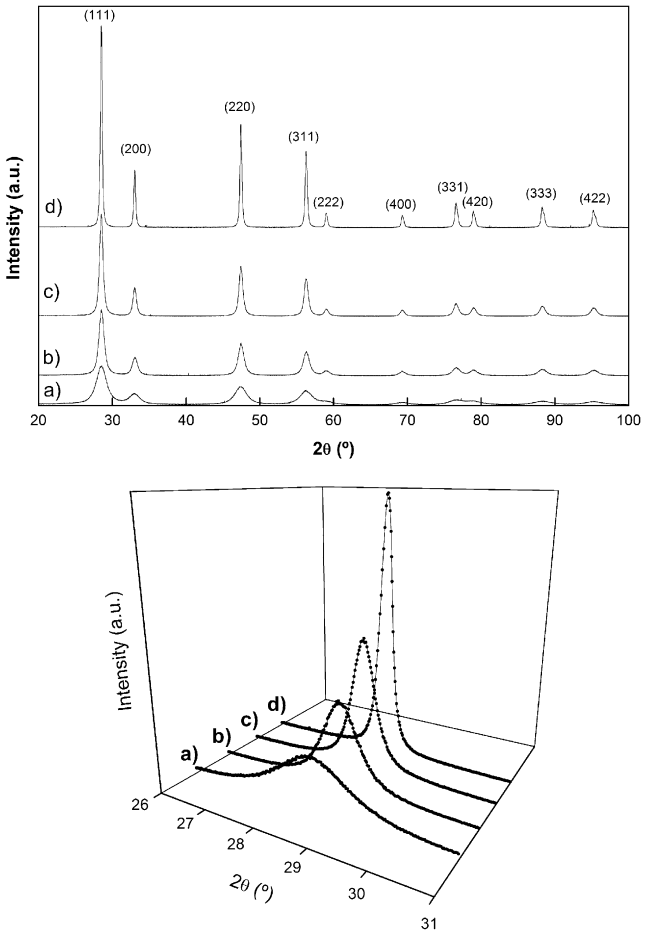

Fig. 4. XRD patterns of nanocrystalline GDC powders calcined for 1 h at (a) 250 °C, (b) 500 °C, (c) 600 °C and (d) 800 °C. The lower plot shows an expansion of the region including the main peak.

with only traces of NO_x, while NO_x, CO and CO_2 are the main gases liberated during the second peak.

From the TGA curve it is possible to identify two steps. The total weight loss up to 350 °C was 71%, whereas after combustion (from 350 °C up to 800 °C), the total weight loss was about 10% of the mass at 350 °C.

X-ray diffraction patterns obtained for the gel precursor calcined at 100, 150, 200 and 250 °C are shown in Fig. 3. These show that the metal complex precursor was amorphous after calcination at 100 and 150 °C, whereas, after its partial decomposition at 200 °C, it is crystalline, some of the main diffraction peaks of GDC being resolved. At 250 °C, all of the characteristic GDC peaks were observed. However, these peaks are relative broad, indicating that the crystallite size was very small.

Table 1
Structural parameters and standard Rietveld agreement factors for nanocrystalline GDC powders calcined at different temperatures. ($Fm\bar{3}m$ space group).

	250 °C	500 °C	600 °C	800 °C
a (Å)	5.41916(8)	5.41911 (4)	5.41809 (2)	5.41728(1)
α (°)	90	90	90	90
V (Å^3)	159.146(4)	159.141(2)	159.052(1)	158.981(1)
R_p	4.48	4.71	4.71	5.59
R_{wp}	6.41	6.99	6.89	8.17
R_e	5.44	5.85	5.73	5.43
χ^2	1.39	1.43	1.45	2.27

Table 2
Average crystallite size (D_{XRD}), specific surface area (A) and calculated primary particle size of GDC powders calcined at different temperatures for 1 h.

$T_{calc.}$/°C	D_{XRD}/nm	A/m^2 g^{-1}	d_{BET}/nm	d/D ratio
250	5.2(1)	49 (1)	17.0	3.3
500	11.0(4)	29.7(6)	28	2.6
600	17.6 (5)	24.9 (3)	33.4	1.9
800	43.7(2)	14.6 (1)	56.9	1.3

Table 3
Carbon content in GDC calcined at different temperatures ($T_{calc.}$) for 1 h.

$T_{calc.}$/°C	Carbon content/%
250	0.56
500	0.21
600	0.13
800	0.07

Table 4
Average crystallite size (D_{XRD}), specific surface area (A) and calculated primary particle size of GDC powders calcined at 500 °C for 1 h with different processing conditions.

Process	D_{XRD}/nm	A/m^2 g^{-1}	d_{BET}/nm	d/D ratio
Wet ball-milled in hexane at 200 rpm for 8 h	10.9(5)	41.8(6)	19.9	1.8
Dry ball-milled at 400 rpm for 1 h	10.7(4)	57.5(3)	14.4	1.4

The extent of peak broadening decreased with increasing calcination temperature, as is shown in Fig. 4. This figure shows the diffractograms of $Gd_{0.1}Ce_{0.9}O_{1.95}$ powder calcined at different temperatures for 1 h. Even after calcination at the highest temperature, 800 °C, the peaks remained relatively broad, indicating that the crystallites were still very small.

A qualitative analysis of the XRD data indicated that all samples exhibited a cubic phase (fluorite type crystal structure. space group $Fm\bar{3}m$), as expected. The structural study was performed using the Rietveld analysis program, FullProf Suite [14]. The $Fm\bar{3}m$ space group was assumed with (Gd^{3+}, Ce^{4+}) cations and O^{2-} anions in 4a and 8c positions, respectively. The lattice parameter a was refined. The peak shape was assumed to be a pseudo-Voigt function. The background of each profile was adjusted by a six-parameter polynomial function in $(2\theta)^n$, $n = 0$–5. In Table 1, the Rietveld analysis results and the standard agreement factors for powders calcined at

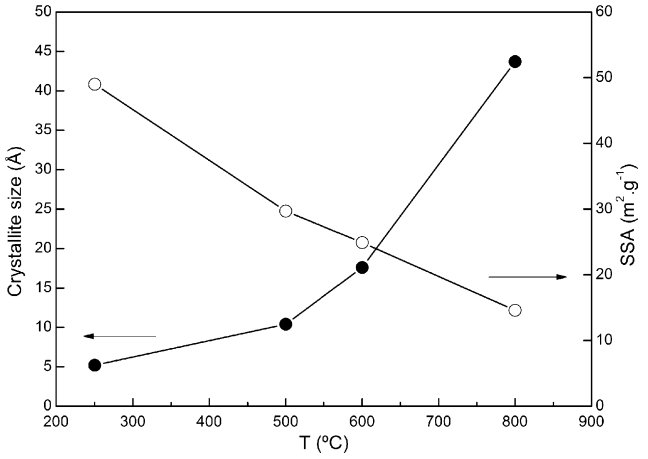

Fig. 5. Average crystallite size obtained from XRD data and SSA of nanocrystalline GDC powders as a function of calcination temperature (for 1 h).

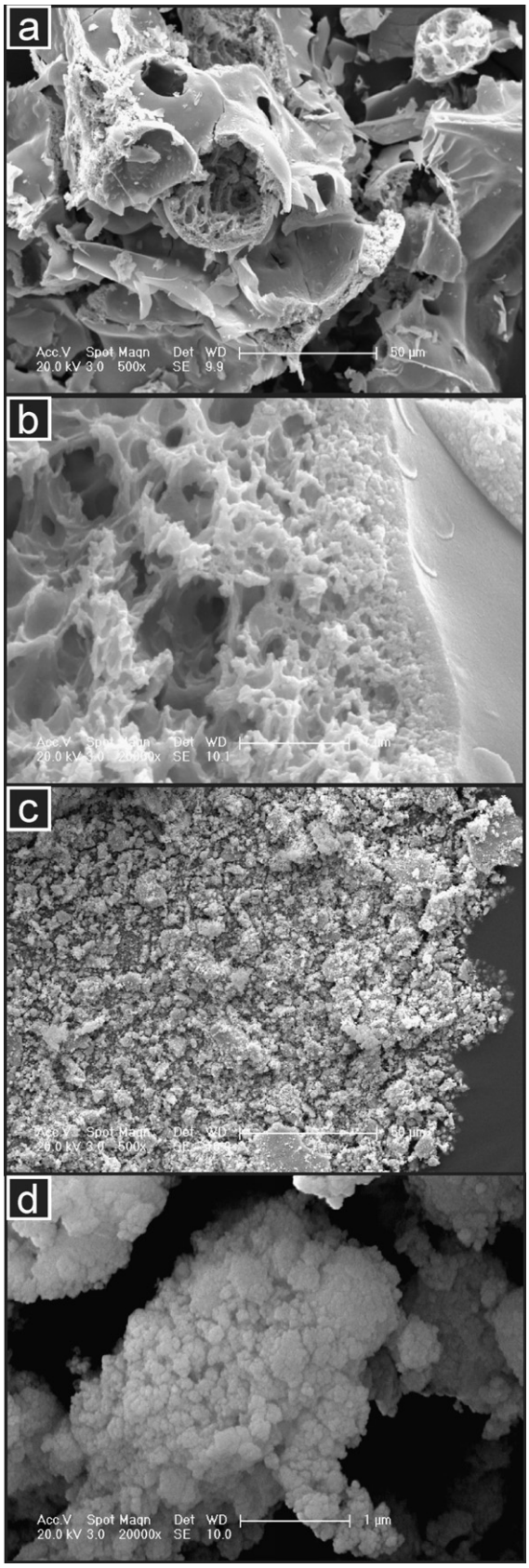

Fig. 6. SEM images of nanocrystalline GDC powders calcined at 500 °C for 1 h. (a and b) As-calcined and (c and d) milled at 400 rpm for 1 h.

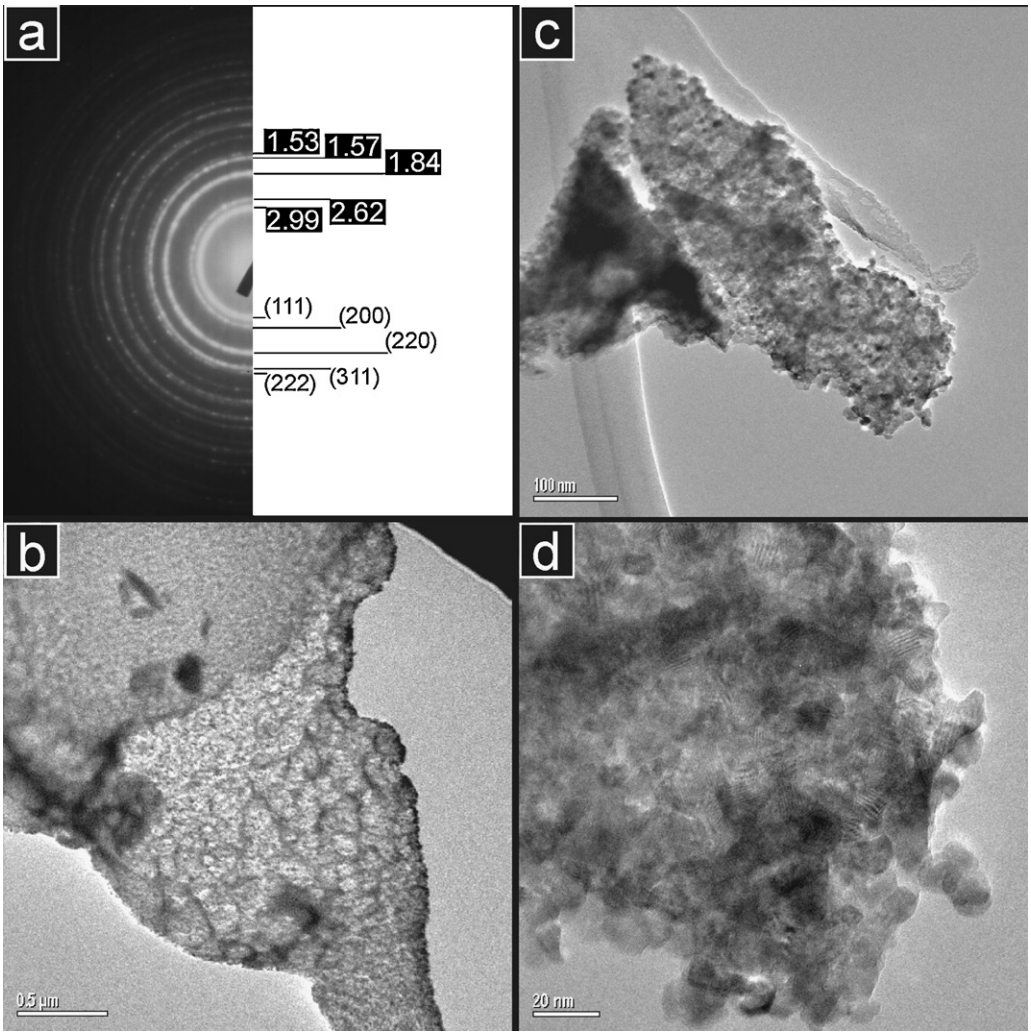

Fig. 7. (a) SAED pattern and (b–d) typical low magnification TEM images of nanocrystalline GDC powder calcined at 500 °C for 1 h. The SAED pattern is labelled with interplanar spacings (in Å) and the corresponding Miller indices of the fluorite structure.

250, 500, 600 and 800 °C are shown. No substantial differences were seen in cell parameter as a function of calcination temperature.

The crystallite size, D, of the calcined powders was estimated using the Scherrer equation, $D = 0.9\lambda/\beta\cos\theta$ where λ is the wavelength of the X-rays (1.5418 Å), θ is the scattering angle of the main reflection (1 1 1) and β is the full width at half-maximum (FWHM) intensity of the corrected peak. The value of the measured FWHM of the silicon standard sample was determined to be 0.110°. The average crystallite sizes are given in Table 2.

Values of the residual carbon content of the GDC powder samples calcined at different temperatures are listed in Table 3. These are relatively low when compared to values obtained for GDC synthesised by combustion methods.

Specific surface area and primary particle size were calculated from the BET data of GDC powders calcined at 500 °C for 1 h and these are given in Table 4 and in Fig. 5. After milling, the powders exhibited significantly higher specific surface area than powders without any mechanical processing. Milled powders were thus expected to exhibit high sinterability.

The SEM images in Fig. 6a and b shows that the as-calcined GDC material were composed of thin sheets in an egg shell-like structure. After milling (Fig. 6c and d), a fluffy powder of obviously small particle size was obtained.

Fig. 7 presents an SAED pattern for the as-calcined GDC powder (500 °C, 1 h). This is completely consistent with the fluorite structure, which was also found in the XRD results. The TEM images in Fig. 7b–d show in more detail the sheet-like structures which were seen at lower magnifications in the SEM images of the powder. It is clear that the sheets consisted of a thin layer of nanoparticles. In the high resolution (HR) TEM images of Fig. 8, the morphology and internal crystal structure of individual nanoparticles is seen. The diameters of a large number (90) of nanoparticles were measured from the HRTEM images. Particle sizes were found to occupy a narrow size range. A histogram showing the distribution of nanoparticle size is presented in Fig. 9. Mean particle size was 7.55 nm (with standard deviation of 3.42 nm) and the mean mass-corrected particle size (weighted for particle mass) was 11.2 nm. The latter value is directly comparable to the value estimated from the XRD data using the Scherrer equation and shows excellent agreement. Individual nanoparticles viewed in the HRTEM images appeared to be single crystals, to exhibit high crystallinity and to have essentially non-defective structures, despite their very small dimensions and relatively low synthesis temperature. Such nanocrystals of GDC are shown in Fig. 8 in four different crystallographic orientations. Digital Diffraction Patterns (DDPs) were calculated by performing a mathematical Fourier transfer on

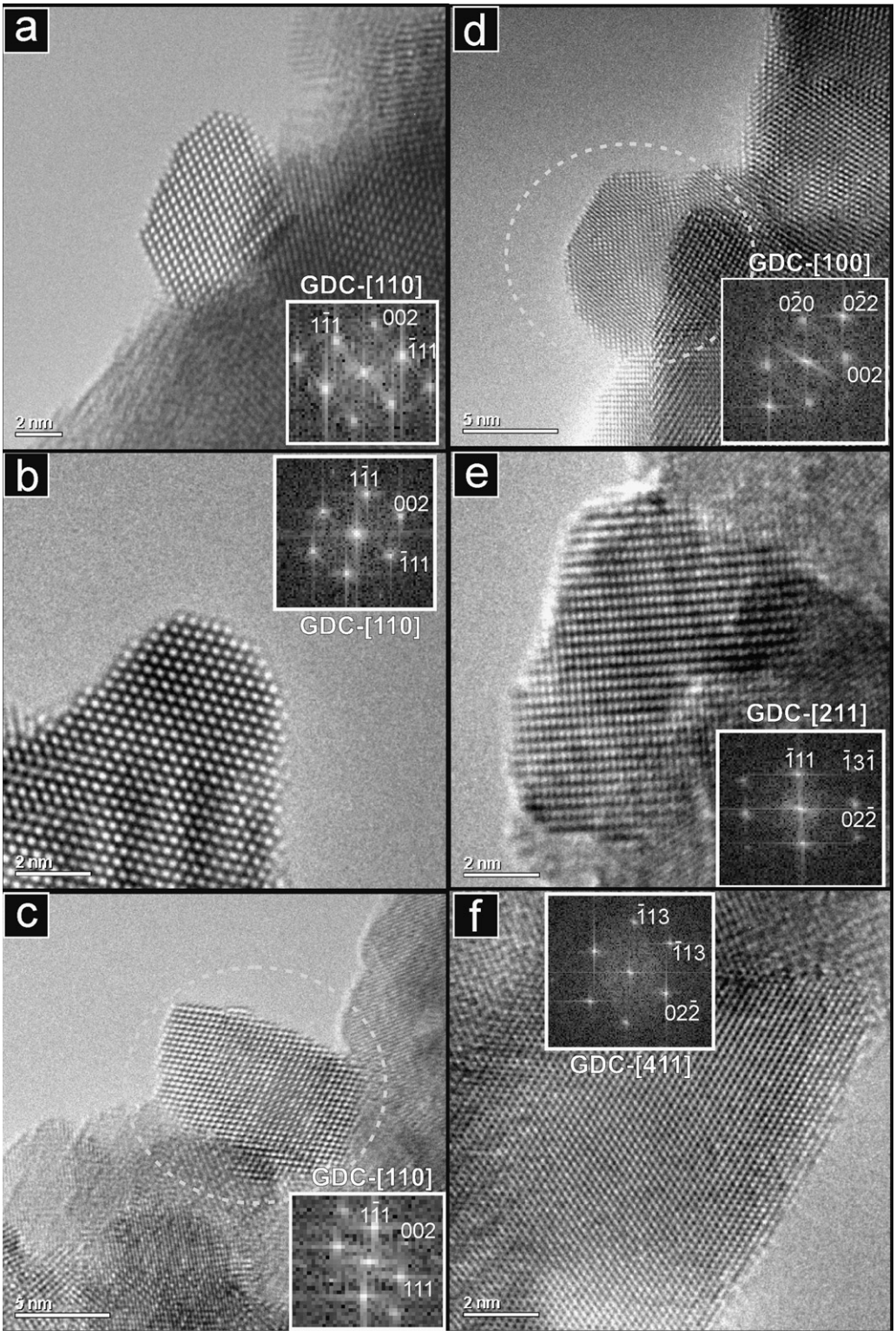

Fig. 8. HRTEM images of GDC calcined at 500 °C for 1 h showing nanocrystals aligned in the (a–c) [1 1 0], (d) [1 0 0], (e) [2 1 1] and (f) [4 1 1] zone axes. DDPs are inset and the diffraction spots are indexed to the fluorite structure.

selected regions of the image and these are inset in the figure. These are indexed to the fluorite structure viewed in the [1 1 0], [1 0 0], [2 1 1] and [4 1 1] zone axes. The effect of ball milling the as-calcined GDC powder at 400 rpm for 1 h is seen in the TEM images of Fig. 10. At low magnifications, the sheet-like structures are much less evident and the secondary structure of the material is considerably more open and less agglomerated than in the unmilled material. The higher magnification images show that the morphology and crystal structure of the individual nanoparticles is no different from those seen in the powder before milling.

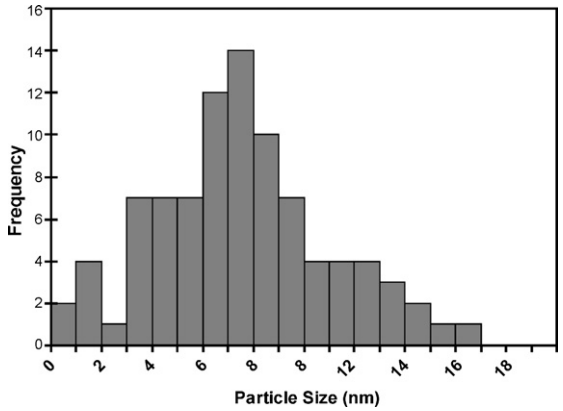

Fig. 9. Histogram showing primary particle size distribution. Particle sizes were measured from the HRTEM images of the GDC sample calcined at 500 °C for 1 h.

3.2. Sinterability

Sintering temperatures, sintering times, relative densities and mechanical processing details of the starting powders are listed in Table 5 for the densified samples. Samples without any mechanical processing exhibited low relative densities (86.1–93.9% of the theoretical density, 7.21 g cm^{-3}), including those samples to which a binder had been added (91.7–94.1%). Densified samples prepared by milling the starting powders at 400 rpm and sintering at low temperature (1300 °C for 30 h) showed relative density of 96.2%. However, when sintered at high temperature – at 1450 °C – these samples exhibited cracking.

Table 5
Powder processing conditions, sintering temperature (T_{sint}) and time (T_{sint}) and relative densities of GDC ceramic samples. Shaded rows refer to samples for which electrical properties are presented.

Sample	Processing conditions	T_{sint}\°C	t_{sint}\h	Relative density\%
GDC-A	500 °C—1 h	1300	8	86.1
GDC-B	500 °C—1 h	1400	8	89.9
GDC-C	500 °C—1 h	1450	8	93.9
GDC-D	250 °C—1 h	1450	8	86.9
GDC-F	600 °C—1 h	1450	8	93.6
GDC-G	800 °C—1 h	1450	8	93.1
GDC-H	500 °C—1 h, 400 rpm	1300	30	96.2
GDC-I	500 °C—1 h, 200 rpm, binder	1300	30	91.7
GDC-J	500 °C—1 h, 200 rpm, binder	1450	8	94.1

The shrinkage behaviour of green GDC pellets prepared from two different powders is shown in the dilatometry plots in Fig. 11. The difference between the two curves is very clear. It can be seen that the pellet prepared from the ball-milled powder (400 rpm, 1 h)

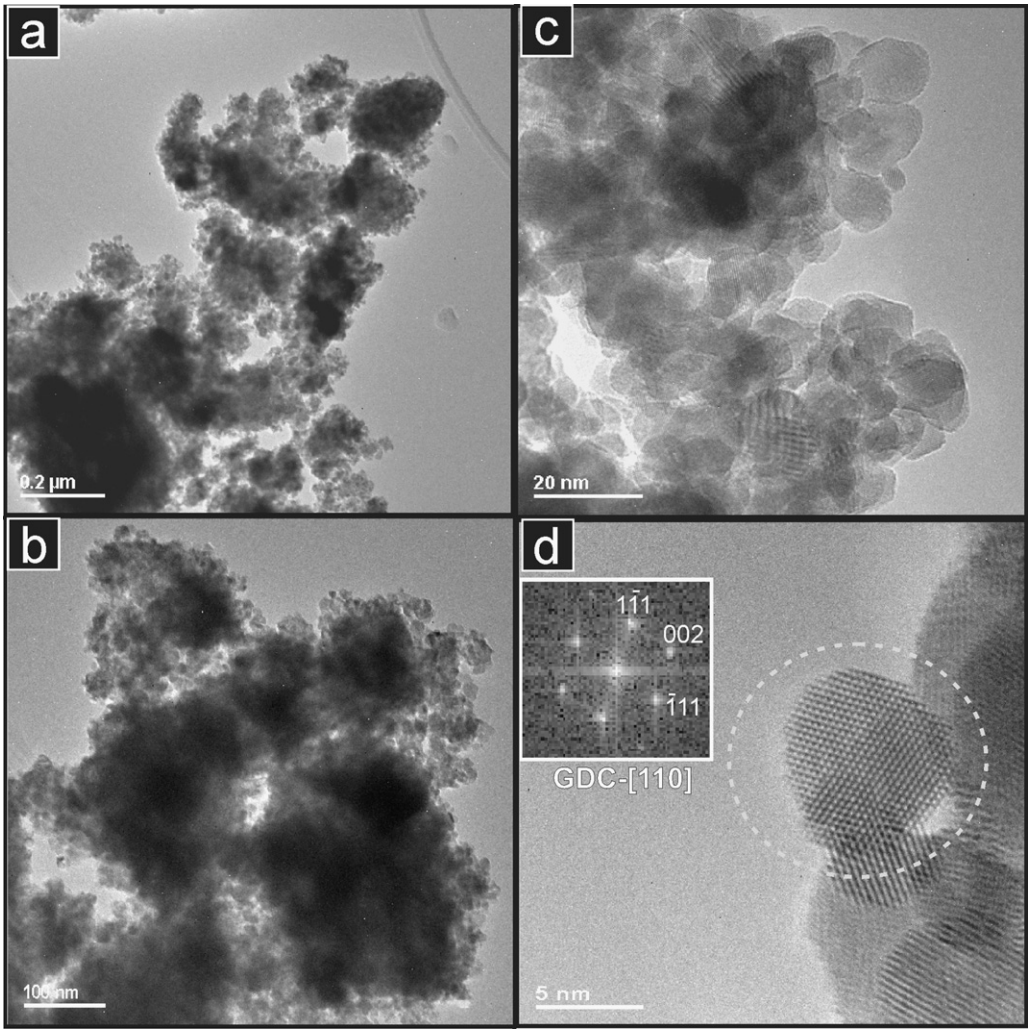

Fig. 10. TEM images of nanocrystalline GDC powder calcined at 500 °C for 1 h and ball-milled at 400 rpm for 1 h: (a and b) low magnification, (c) intermediate magnification and (d) HRTEM image showing a nanocrystal aligned in the [1 1 0] zone axis. The corresponding DDP is inset and the diffraction spots are indexed to the fluorite structure.

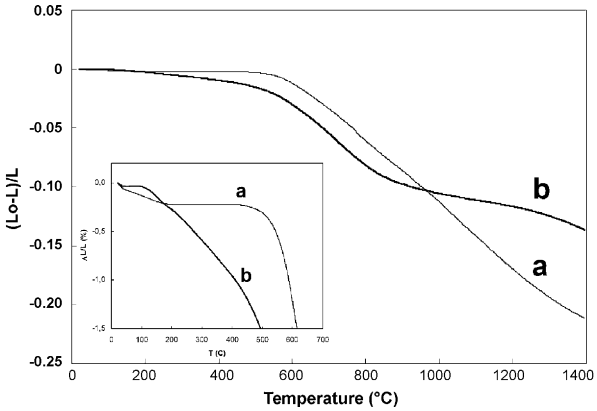

Fig. 11. Linear dilatometry curves of relative length change $(L_0 - L/L)$ against temperature for compacted $Gd_{0.1}Ce_{0.9}O_{1.95}$ powders calcined at 500 °C for 1 h (a) without milling and (b) milled at 400 rpm for 1 h.

started to shrink at a lower temperature than the sample prepared from the unmilled powder. It is important to note that the densities of these green pellets were 54% and 63% of theoretical density for the unmilled and ball-milled preparations, respectively. The final relative density values are shown in Table 5 (GDC-C and GDC-H).

The single crystal phase was confirmed by XRD for sintered samples. As an example, the XRD pattern of a dense $Gd_{0.1}Ce_{0.9}O_{1.95}$ pellet sintered at the highest temperature, 1450 °C, for 8 h, is given in Fig. 12. This can be indexed to the fluorite structure and shows no impurity peaks. Therefore the single fluorite phase had been preserved. The XRD pattern also indicates an increase in grain size and in crystallinity.

Average grain sizes were determined from SEM micrographs of cross-sectional fracture surfaces of the sintered pellets (Fig. 13). These were about 0.4–0.7 μm, after sintering at 1300 °C for 30 h, and 0.9–1.2 μm after sintering at 1450 °C for 8 h. The average grain size was thus seen to increase with increasing sintering temperature.

3.3. Electrical properties

Fig. 14 shows a typical impedance spectrum (an Nyquist plot) of GDC, in this case, recorded at 200 °C and corresponding to a sintered pellet of GDC-A. The contributions of the bulk, grain boundary and electrode processes can be clearly identified in the figure at high, intermediate and low characteristic frequencies, respectively. The impedance spectra were fitted to the conventional equivalent

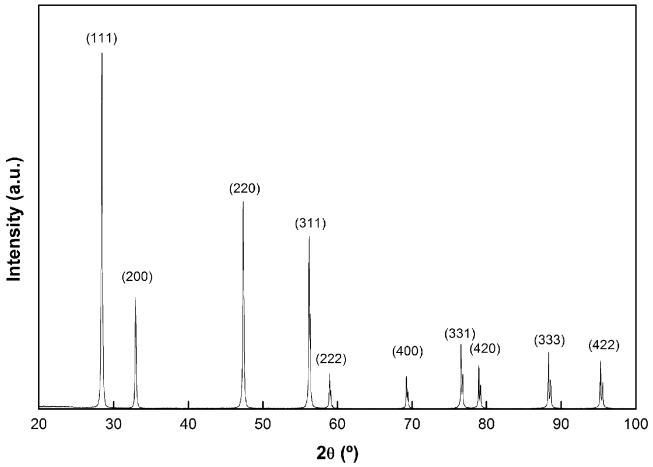

Fig. 12. XRD pattern of GDC sintered at 1450 °C for 8 h (GDC-C).

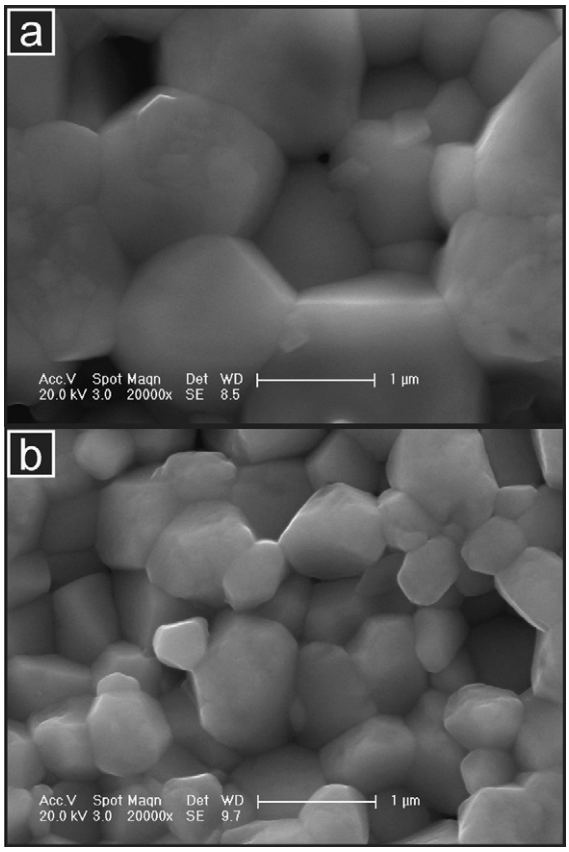

Fig. 13. SEM images of cross-sectional fracture surfaces of GDC samples sintered: (a) at 1450 °C for 8 h (GDC-C) and (b) at 1300 °C for 30 h (GDC-H).

circuit shown in the figure. This consists of three R-CPE (Resistor-Constant Phase Element) sub-circuits connected in series and gives rise to three arcs in the Nyquist plot. This equivalent circuit was used only to obtain the best fit to the experimental data and to determine adequately the electrolyte resistance. It was not used to explain the kinetics of the redox reactions at the electrodes. As

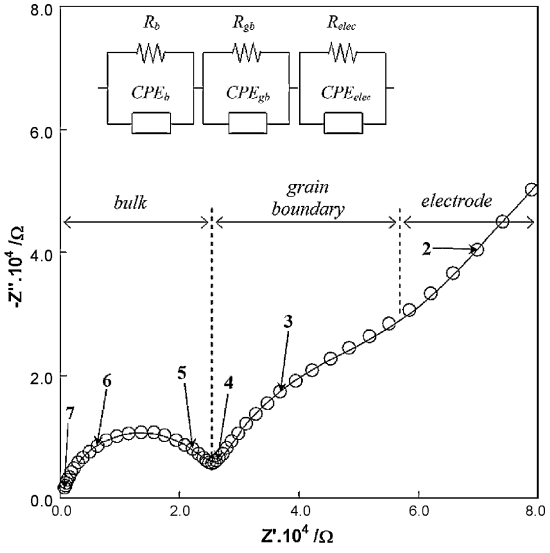

Fig. 14. Nyquist plot recorded at 200 °C of GDC pellet sintered at 1300 °C for 8 h (GDC-A). The solid line shows the total fit and the labels indicate the decimal logarithm of frequency (Hz).

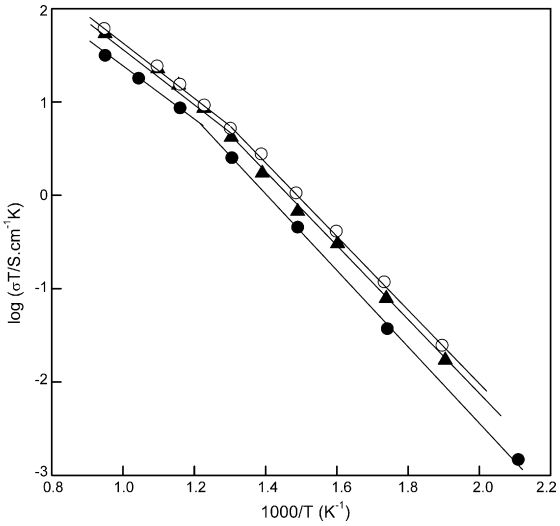

Fig. 15. Arrhenius-type plot of total conductivity of ceramic GDC samples sintered with different sintering programs: GDC-A (●), GDC-C (▲) and GDC-H (○).

measurement temperature is increased, the characteristic frequencies of the bulk, grain boundary and electrode processes increase and may fall outside the frequency range of the instrument. For this reason, in the impedance spectra of GDC, the arc corresponding to the bulk contribution was seen to disappear at measurement temperatures above 350 °C. At higher temperatures, around 500 °C, the grain boundary arc also disappeared.

Arrhenius-type plots of total conductivity derived from these impedance spectra are presented in Fig. 15 for samples sintered either at 1300 °C for 8 h (GDC-A), at 1450 °C for 8 h (GDC-C) or at 1300 °C for 30 h (GDC-H). For all three samples, the plots consist of two sections of different gradient with an inflection occurring at around 500 °C. This indicates that there were significant differences in conduction mechanism at low (200–500 °C) and at high (500–800 °C) temperatures. The activation energy (E_a) of the total conductivity (σ) was derived from the impedance data using the Arrhenius law: $\sigma = \sigma_0/T \exp(-E_a/kT)$ where σ_0 is the pre-exponential factor and k is the Boltzmann constant. In Table 6, the activation energies for total conductivity of $Gd_{0.1}Ce_{0.9}O_{1.95}$ ceramics sintered following different treatments are listed. The change in gradient, and so in activation energy, observed at around 500 °C can be explained by changes in the behaviour of the defects in the GDC material. The low temperature behaviour is affected by the association of defects to form ($Gd'_{Ce} - V_O^{\bullet\bullet}$) complexes. As the temperature rises above 500 °C, these complexes become dissociated, and the activation energy of total conduction falls to lower values [1,15].

In Table 6 and Fig. 15 it can be seen that samples with the highest densities exhibited the highest total conductivity values. Moreover, the activation energy values for the two denser samples (GDC-H and GDC-C) are similar. A slight difference is observed for the GDC-A sample which has a lower density and a slightly higher activation energy, for temperatures <500 °C, than for the denser samples. This

Table 6
Activation energies (E_a) for total conductivity of GDC ceramics sintered with different treatments. Total conductivity values at 600 °C ($\sigma_{600\,^\circ C}$) were extrapolated from the Arrhenius plots.

Sample	E_a (<500 °C)/eV	E_a (>500 °C)/eV	$\sigma_{600\,^\circ C}$/S cm^{-1}
GDC-A	0.80(4)	0.53(2)	$1.091(4) \times 10^{-2}$
GDC-C	0.78(3)	0.56(1)	$1.793(3) \times 10^{-2}$
GDC-H	0.78(4)	0.57(1)	$1.918(3) \times 10^{-2}$

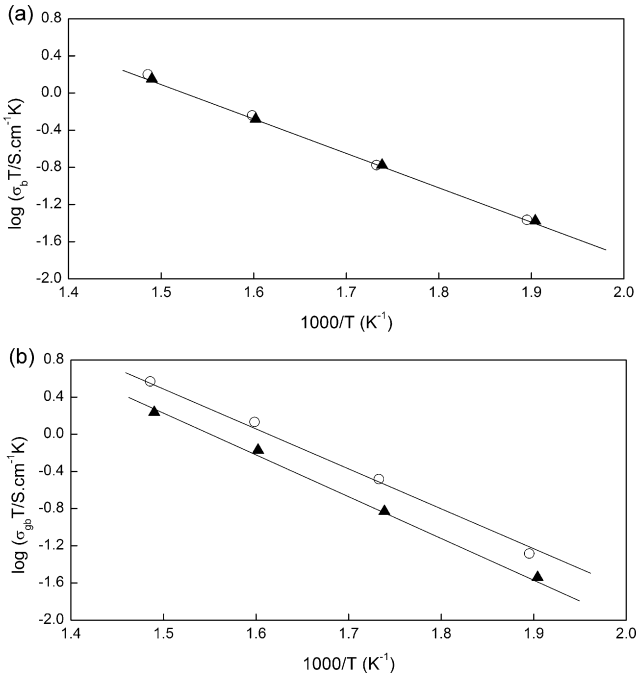

Fig. 16. Arrhenius-type plot of (a) bulk conductivity and (b) grain-boundary conductivity of ceramic GDC samples sintered with different sintering programs: GDC-C (▲) and GDC-H (○).

is in good agreement with previous work reported in the literature [16,17].

Total conductivity values at 600 °C were extrapolated from the Arrhenius plot (Fig. 12) and are shown in Table 6. Total conductivity is seen to increase with increasing sample density, being lowest for GDC-A, significantly higher for GDC-C and slightly higher again for GDC-H. These values of total conductivity are in good agreement with those reported in the literature, which range from 1.0 to 2.5×10^{-2} S cm^{-1}. The highest value, reported by Steele [1], was obtained for a commercial powder sintered at a relatively high temperature (1400 °C). Other methods used to obtain dense GDC samples with good electrical properties, such as gel-casting [5], a low-temperature solution route [15] and mechanochemical synthesis [16], gave rise to values of total conductivity at 600 °C of 2.3, 1.4 and 1.0×10^{-2} S cm^{-1}, respectively. In the current work, the highest total conductivity at this temperature was for the sample prepared from milled powders (GDC-H), at 1.91×10^{-2} S cm^{-1}.

Arrhenius-type plots of bulk and grain boundary conductivity of GDC-C and GDC-H are shown in Fig. 16a and b, respectively. Interestingly, the bulk conductivity for both samples is essentially the same, exhibiting similar activation energies (0.76 eV). This indicates that no significant change in composition or phase of the bulk material was caused by prolonged thermal treatment, and that the two sintering methods resulted in chemically identical bulk material.

The grain boundary conductivity (Fig. 16b), however, does show changes. Firstly, the grain boundary conductivity of the material sintered at the higher temperature (GDC-C) is considerably lower than for the material sintered at the lower temperature (GDC-H). A slight difference is also observed in the activation energy of the grain boundary conductivity: the GDC-C sample exhibits a value of about 0.93 eV, while the value for GDC-H is 0.90 eV.

These changes in grain boundary conductivity are likely to be caused by the accumulation of impurities, such as Si, at the grain boundaries during materials preparation. Interestingly, the difference in behaviour between GDC-C and GDC-H could be caused by homogenization of the impurity distribution in GDC-H during the

milling step, making it less likely for impurities to be accumulated at the grain boundaries during the subsequent thermal treatment. Another important factor is the high temperature employed to sinter the GDC-C sample (unmilled powder), which would be expected to accelerate segregation of Si to the grain boundaries.

The ability of SiO_2 impurities to cause a decrease in grain boundary conductivity has been recognised in ceria-based ceramics. According to Steele [1], the grain boundary effect for clean GDC cannot be detected above 500 °C. However, it dominates the total conductivity up to 1000 °C for impure GDC samples. Therefore, studies on the total conductivity would be affected by these grain boundary phenomena [18].

4. Conclusions

An effective, inexpensive method for preparing nanometric GDC is presented. The gel precursor was shown to calcine via a two-step mechanism to form powder material consisting of thin layers in an egg shell-like secondary structure. The XRD and TEM results showed that the synthesised powder possessed the expected crystal structure, was single-phase and had good crystallinity. Average particle size was estimated from the peak broadening in the XRD patterns and was measured directly in TEM. These two methods were in excellent agreement, giving a value of 11 nm for the powder calcined at 500 °C for 1 h. In HRTEM, particle size was seen to occupy a narrow size range and the crystal structure of the particles was seen to be essentially non-defective. Samples prepared from the milled nanopowders possessed excellent sinterability at relatively low temperature (1300 °C) and the resulting ceramics exhibited the highest densities. The electrical conductivity of pellets sintered from the GDC powder was measured using impedance spectroscopy. The total ionic conductivity of GDC samples with the highest density was comparable with the best values reported in literature using a soft-chemical method. At 600 °C, the highest total conductivity was 1.91×10^{-2} S cm^{-1} for the sample prepared from milled powders.

Acknowledgements

This work was carried out within the UK EPSRC SUPERGEN Fuel Cell consortium. Electron microscopy was carried out at the Electron Microscopy Facility, University of St Andrews (TEM) and at the CHIPS Facility, University of Dundee (SEM).

References

[1] B.C.H. Steele, Solid State Ionics 129 (2000) 95–110.
[2] S. Wang, T. Kobayashi, M. Dokiya, T. Hashimoto, Journal of the Electrochemical Society 147 (10) (2000) 3606–3609.
[3] A. Sin, Y. Dubitsky, A. Zaopo, A.S. Arico, L. Gullo, D. La Rosa, S. Siracusano, V. Antonucci, C. Oliva, O. Ballabio, Solid State Ionics 175 (2004) 361–366.
[4] T.S. Zhang, J. Ma, S.H. Chan, J.A. Kilner, Solid State Ionics 6 (2005) 377–384.
[5] J.-G. Cheng, S.-W. Zha, J. Huang, X.-Q. Liu, G.-Y. Meng, Materials Chemistry and Physics 78 (2003) 791–795.
[6] B. Rambabu, S. Ghosh, H. Jena, Journal of Materials Science 41 (22) (2006) 7530–7536.
[7] E. Ruiz-Trejo, J. Santoyo-Salazar, R. Vilchis-Morales, A. Benítez-Rico, F. Gómez-García, C. Flores-Morales, J. Chávez-Carvayar, G. Tavizón, Journal of Solid State Chemistry 180 (2007) 3093–3100.
[8] T. Mahata, G. Das, R.K. Mishra, B.P. Sharma, Journal of Alloys and Compounds 391 (1–2) (2005) 129–135.
[9] R.A. Rocha, E.N.S. Muccillo, Materials Research Bulletin 38 (15) (2003) 1979–1986.
[10] E.N.S. Muccillo, R.A. Rocha, R. Muccillo, Materials Letters 53 (2002) 353–358.
[11] T.S. Zhang, J. Ma, Y.J. Leng, J.A. Kilner, Journal of the Crystal Growth 274 (2005) 603–611.
[12] D.P. Fagg, J.C.C. Abrantes, D. Perez-Coll, P. Nunez, V.V. Kharton, J.R. Frade, Electrochimica Acta 48 (2003) 1023–1029.
[13] D. Perez-Coll, P. Nunez, J.C. Ruiz Morales, J. Pena-Martinez, J.R. Frade, Electrochimica Acta 52 (5) (2006) 2001–2008.
[14] J. Rodríguez-Carvajal, (1998). FullProf98, Version 0.2. Laboratoire León Brillouin (CEA-CNRS), Saclay, France.
[15] Y.B. Go, A.J. Jacobson, Chemistry of Materials 19 (2007) 4702–4709.
[16] K. Maca, J. Cihlar, K. Castkova, O. Zmeskal, H. Hadraba, Journal of the European Ceramic Society 27 (10) (2007) 4345–4348.
[17] V.V. Ivanov, V.R. Khrustov, Y.A. Kotov, A.I. Medvedev, A.M. Murzakaev, S.N. Shkerin, A.V. Nikonov, Journal of the European Ceramic Society 27 (2006) 1041–1046.
[18] T.S. Zhang, J. Ma, S.H. Chan, P. Hing, J.A. Kilner, Solid State Science 6 (2004) 565–572.